Economic Geology
Vol. 97, 2002, pp. 819–826

Hyperspectral Mapping of Mineral Assemblages Associated with Gold Mineralization in the Central Pilbara, Western Australia

Phil Bierwirth,†

Department of Geology, Australian National University, Canberra, ACT 0200, Australia

David Huston, and Richard Blewett

Minerals Division, Geoscience Australia, GPO Box 378, Canberra, ACT 2601, Australia

Abstract

The Indee district, located in the Central Pilbara tectonic zone of the North Pilbara terrain in Western Australia, contains Archean lode gold deposits and epithermal gold systems. Hydrothermal alteration assemblages associated with these deposits contain the minerals pyrophyllite, white mica, chlorite, and tourmaline. Known prospects are surrounded by flat areas of poorly exposed calcretized bedrock, calcretes, rock float, and sandy soils. Two adjacent lines of airborne hyperspectral data (HyMap®) were acquired. To produce mineral abundance maps, these data were processed to correct for atmospheric and illumination conditions and then calibrated to reflectance data using field spectra. This analysis successfully mapped the distribution of pyrophyllite, white mica, Mg chlorite, Fe chlorite, calcite, dolomite, kaolinite, tourmaline, hematite, and goethite. Alteration assemblages associated with the Camel 2 deposit, which is located along the Mallina shear zone, were found to be characterized by pyrophyllite and Al-rich white mica, the latter having an AlOH absorption feature at 2.194 μm. In contrast, alteration assemblages associated with epithermal deposits south of the Mallina shear zone are characterized by Al-poor white mica with a longer wavelength absorption feature at 2.210 μm, the shift reflecting the change in Al chemistry (Tschermak substitution). Tourmaline is also present near the epithermal-like deposits, suggesting that it may be an integral part of these systems. Fe chlorite is associated with both the mesothermal and epithermal systems but is also pervasive as a regional metamorphic mineral. Regolith-related carbonates are common throughout the area and their compositions are determined by the hyperspectral processing. Mineral abundance images were verified by PIMA® (portable infrared mineral analyser) analysis of ground samples, and assays of rocks in previously unknown areas of pyrophyllite and white mica confirmed the presence of anomalous gold. These results show that mineral maps and compositional information derived from hyperspectral analysis are extremely valuable for exploration, even in poorly exposed, regolith-dominated districts such as Indee.

Introduction

The recent development of remote hyperspectral systems offers a potential boon to mineral exploration as these instruments can be used to map the distributions of many minerals diagnostic of fluid-rock interaction. The aim of this study is to assess the use of airborne hyperspectral data to map the distribution of both primary alteration and regolith minerals associated with different styles of gold mineralization in the Indee district (Fig. 1), which is a part of the Central Pilbara tectonic zone in Western Australia. The Indee district was chosen for this study because the poor bedrock exposure tests the applicability of remote hyperspectral imaging for enhanced mineral mapping in regolith-dominated environments.

Regional Geology

The Central Pilbara tectonic zone is the youngest part of the mainly Paleo- to Mesoarchean North Pilbara terrain (Fig. 1). It formed between ca. 3020 and 2940 Ma as a basin between the older East and West Pilbara granite-greenstone terranes. This basin comprises the Whim Creek greenstone belt and the adjacent Mallina basin (Van Kranendonk et al., 2002). Although a few small Sb-Au deposits are known in the Whim Creek greenstone belt, the most significant Au-bearing deposits occur in the Mallina basin (Huston et al., 2002a).

† Corresponding author: e-mail, philb@geology.anu.edu.au

The Mallina basin consists mainly of turbiditic sandstone, siltstone, and shale of the Constantine Sandstone and Mallina Formations, with minor high Mg basaltic sills and flows. The Mallina basin has been intruded by granitoids at ca. 2950, 2935, and 2925 Ma (Fig. 1). Three major deformation events have affected the Central Pilbara tectonic zone. The first and third events both produced steeply dipping, east-northeast–trending fabrics and tight folds, whereas the second event produced north-trending fabric and folds (Smithies, 1999; Blewett, 2002). However, the most important structure in the Mallina basin is the Mallina shear zone, a 1-km-wide, east-trending zone of anastomosing shears that bisects the Mallina basin (Fig. 2a, Smithies, 1999).

Topographically the Indee district is flat (Fig. 3a, b), with isolated hills containing the main outcrops. Outside these hills, the surface is dominated by lag deposits and lesser calcrete. The trace of the Mallina shear zone is marked by a low calcretized ridge. The outcrop exposure is minimal and the area is dominated by essentially in situ soil and residual rock float.

Deposits of the Indee District

Although one of the first gold discoveries in Western Australia was made at the Mallina homestead (Fig. 1), the full potential of the Indee district for gold was only realized recently with the discovery of the Withnell, Camel 1, and Camel 2

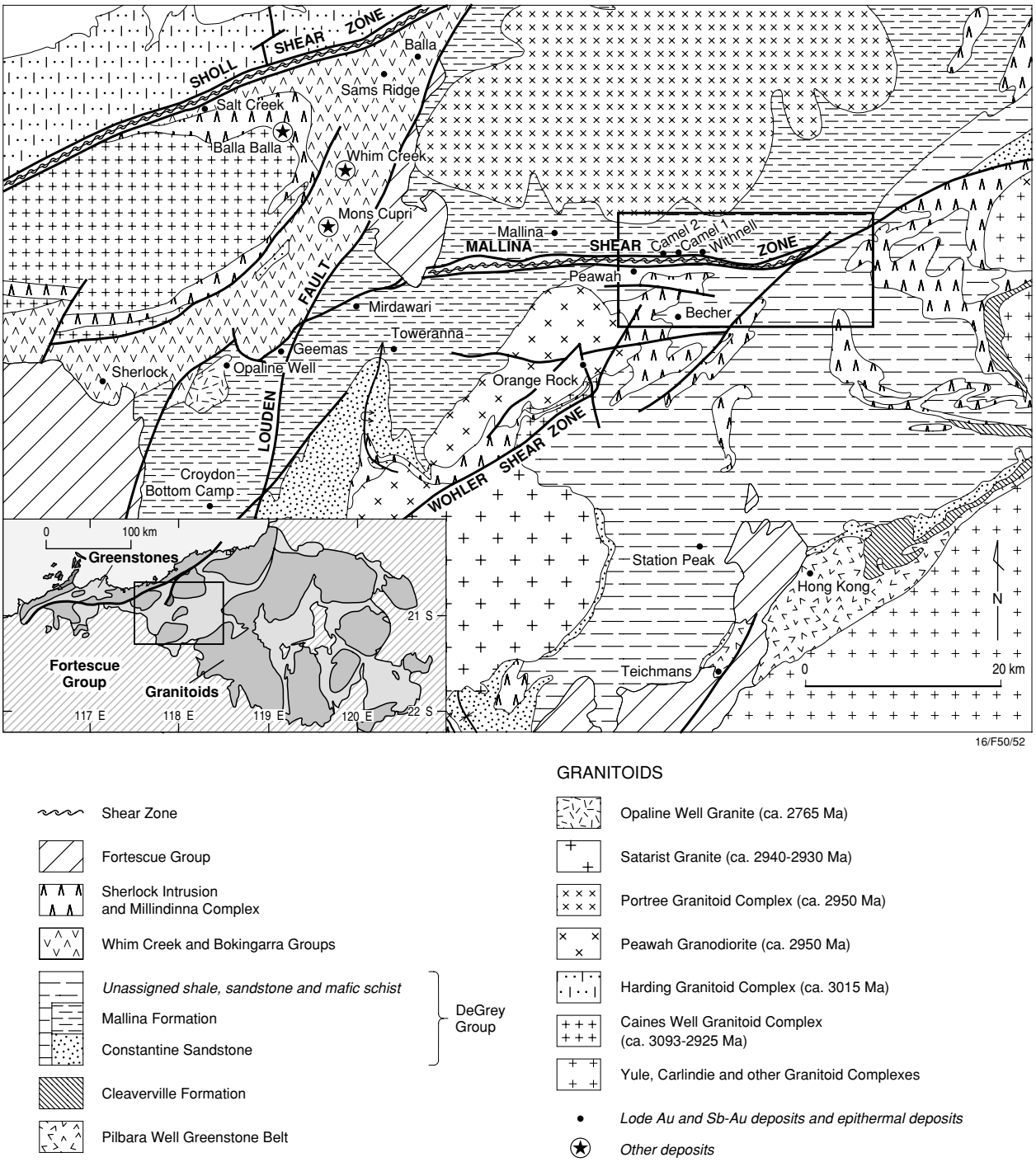

FIG. 1. Geologic map of the Central Pilbara tectonic zone and the location of the HyMap® survey and study area.

gold prospects in the late 1990s. These prospects have a combined geologic resource of 4.96 million metric tons (Mt), grading 2.08 g/t Au (Australian Registry of Mining, 2001).

Huston et al. (2002a) have documented a large variety of prospects in the Indee district (Fig. 1), identifying four types: (1) lode Au deposits associated with quartz-white mica-carbonate ± feldspar alteration assemblages (e.g., Withnell); (2) Au deposits associated with pyrophyllite-bearing alteration assemblages (e.g., Camel 2); (3) lode Sb-Au deposits associated with quartz-white mica alteration assemblages (e.g., Peawah); and (4) epithermal-like vein deposits with anomalous Au, Sb, and As associated with quartz-white mica alteration assemblages (e.g., Becher).

The first two types of deposits appear to be the most significant and are spatially associated with the Mallina shear zone (Figs. 1, 2a). The third type is also locally associated with

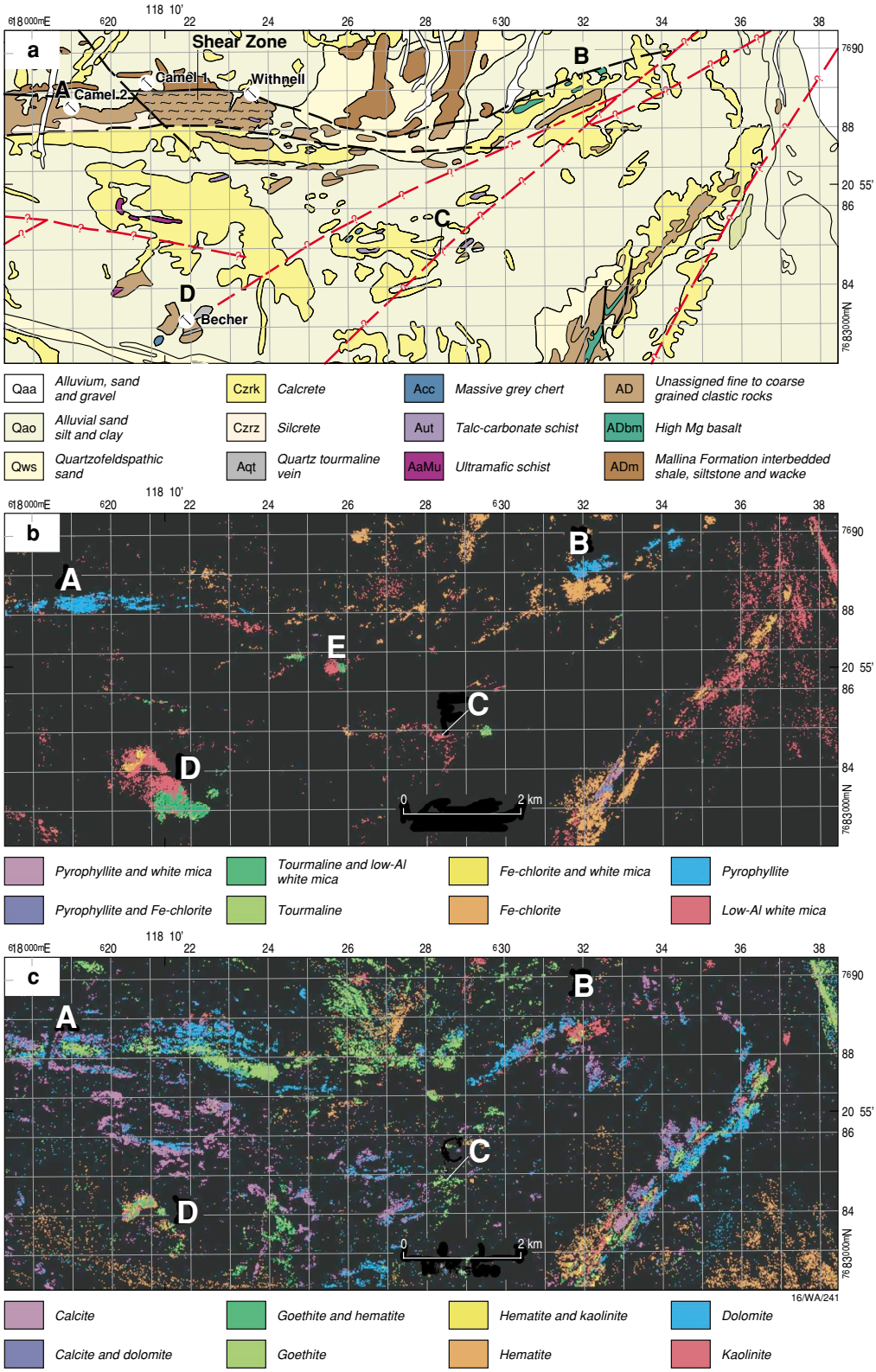

FIG. 2. a. Geology of the Mallina HyMap® survey area. Brown areas are metasediments of the Archean Mallina Formation. Green and purple units are mafic to ultramafic igneous rocks. Bright yellow areas are calcrete, paler yellow areas are sandy soil. From Smithies (1999). Grid lines are at 1 km. Location of Camel 2 (A), Becher (D), Camel 1, and Withnell are also shown. Points B and C are unnamed anomalies discussed in the text. b. Distribution of minerals associated with gold and hydrothermal alteration, derived by analysis of hyperspectral data. Site E is a potential target with a small zone of tourmaline adjacent to a low Al white mica anomaly. c. Regolith and weathering mineral distribution derived from HyMap® data.

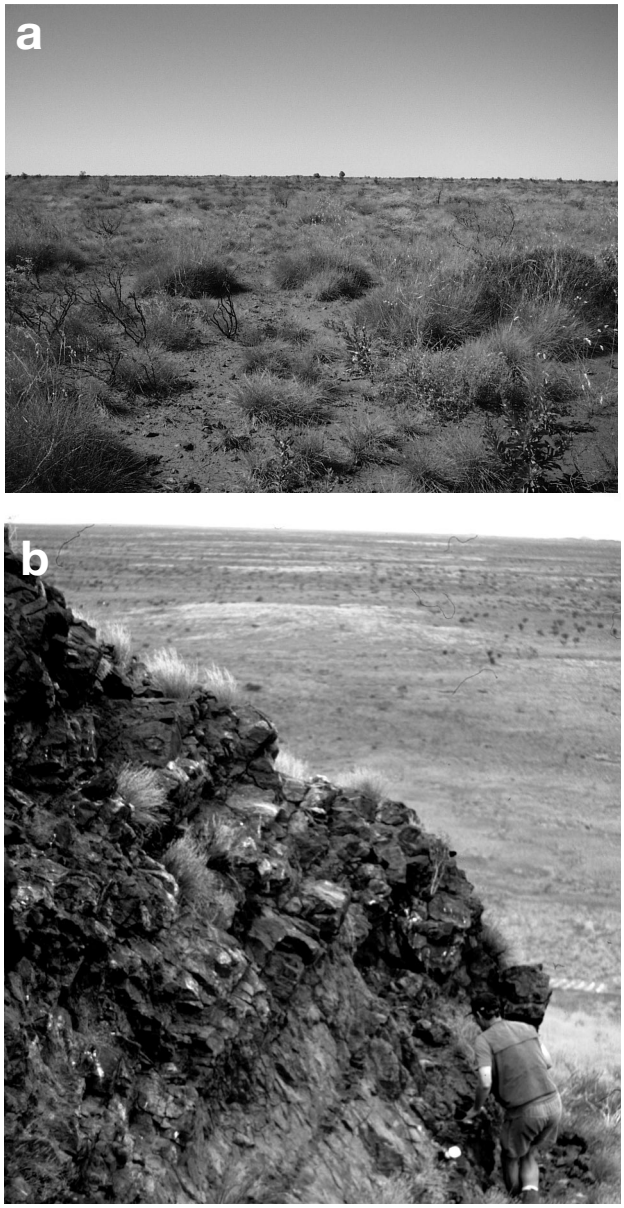

FIG. 3. a. Outcrop view of typical regolith-dominated Indee district. Photograph taken at site B. b. View east over a tourmalinite ridge at Becher. Note the very flat background landscape.

the Mallina shear zone, whereas the fourth, epithermal type, is not associated with the Mallina shear zone. Huston et al. (2002b) infer that deposit types one to three formed at around 2900 Ma, possibly in association with local D_3, whereas the epithermal-like deposits formed at around 2750 Ma, possibly in association with the opening of the Late Archean Hamersley province.

Data Acquisition and Analysis

To determine the effectiveness of hyperspectral imaging for mapping alteration assemblages associated with the gold deposits, two adjacent lines of airborne HyMap® data were acquired over the most intensely mineralized portion of the Indee district at 10-m pixel resolution (Fig. 1). The HyMap® system is flown by HyVista Corporation Pty. Ltd. on a fixed-wing aircraft typically at an altitude of about 2.5 km. The sensor collects reflected solar radiation in 128 bands covering the 0.440- to 2.500-μm wavelength range, including the visible to near-infrared (VNIR) and short-wave infrared (SWIR) regions of the electromagnetic spectrum (Cocks et al., 1998). The airborne data were supplemented by analysis of samples from the area with the PIMA® and the FieldSpec analytical spectral devices (ASD)® spectrometers. The PIMA® measures reflected radiation in the range of 1.3 to 2.5 μm while the FieldSpec ASD® measures the same from 0.35 to 2.5 μm. For both instruments, raw radiance data are corrected to reflectance by reference to a spectralon reflectance standard.

Results of Field Spectral Analysis

One hundred and twenty-eight rock and soil samples were collected from known alteration zones, lithologies, and regolith types in the area. Some preliminary processing of the HyMap® data, using the methods described in the next section, was used to aid the siting of traverses and point samples. From these samples, 180 PIMA® and 63 FieldSpec ASD® measurements were obtained. Rock samples were commonly measured from both weathered and fresh surfaces. Minerals identified by the PIMA® spectrometer include pyrophyllite, Al-poor to Al-rich white mica, kaolinite, opal, calcite, dolomite, Fe chlorite, Mg chlorite, tourmaline, and serpentine. The presence of pyrophyllite and tourmaline as well as carbonate and chlorite compositions was confirmed by X-ray diffraction (XRD) analysis. Sample spectra indicating the strong presence of these minerals are shown in Figure 4 and these samples are relatively pure. Figure 4a also shows spectra for green and dry vegetation samples collected from the field area.

Minerals associated with hydrothermal alteration in this area include pyrophyllite, Al-poor white mica, Fe chlorite, and tourmaline. The main spectral absorption feature for pyrophyllite is the AlOH absorption at 2.166 μm (Fig. 4b). Sericite composition varies across the area and Figure 3c shows two end members with the AlOH feature at 2.194 (muscovite) and 2.210 μm (phengite), respectively. The shift to longer wavelengths is associated with Mg-Fe-Si substitution for Al (Duke, 1994).

Figure 4b shows the spectral features of chlorite end members found in the survey area. An increase in Mg substitution results in a decrease in intensity of the 2.250-μm feature and a slight shift to a shorter wavelength (McLeod et al., 1987). The MgOH feature is broader and more intense and has shifted to 2.330 μm compared to 2.350 μm for Fe chlorite. The shift of the OH feature from 1.41 to 1.395 μm is also consistent with an increase in Mg substitution (McLeod et al., 1987). Mg chlorite can be confused with other minerals such as epidote and dolomite. For these spectra, the presence of chlorite was confirmed by XRD analysis and the relative Fe/Mg composition was confirmed by XRD peak intensities. The Mg chlorite spectrum in Figure 4b was obtained from a sample that contained minor quartz, dolomite, and calcite, the impurities perhaps explaining why the small expected feature at 2.39 μm is not apparent. As well as being associated with hydrothermal alteration, Fe chlorite is found in unaltered but regionally metamorphosed sedimentary rocks

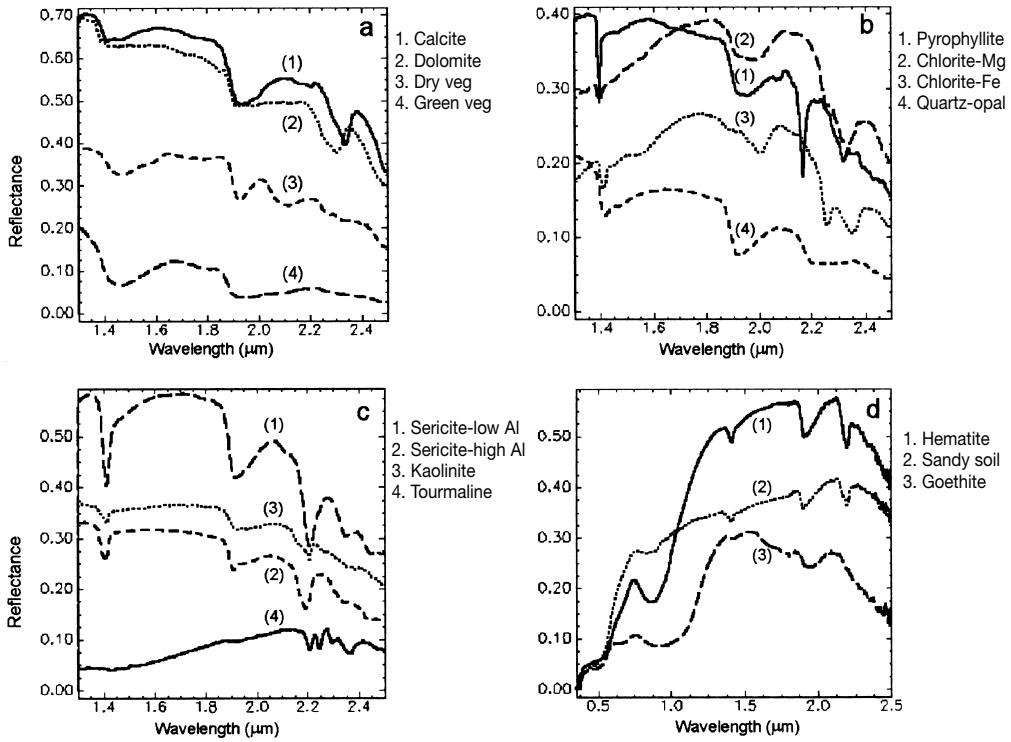

FIG. 4. PIMA® spectra of minerals and vegetation from samples collected in the Mallina study area (see text for discussion).

typically in association with kaolinite as a weathering product. Altered sedimentary rocks contain Fe chlorite but generally in association with white mica. Fe and Mg chlorite are common for basic rocks in the area. The tourmaline features shown in Figure 4c are characteristic of the tourmaline species schorl.

Other minerals have formed in the regolith through weathering processes. Carbonates associated with calcretes vary in composition from magnesium rich (magnesite, dolomite) to calcium rich (calcite). The main carbonate spectral feature (Fig. 4a) varies according to the dominant cation from 2.308 (magnesite) to 2.340 μm (calcite). The opaline silica spectrum (Fig. 4b) was obtained from silcrete and has only broad spectral features. Kaolinite is a common weathering mineral and the infrared spectrum (Fig. 4c) has a sharp characteristic feature at 2.21 μm and a shoulder at 2.166 μm, indicating low crystallinity.

Full spectrum FieldSpec ASD® analysis of representative rock samples shows VNIR features of Fe oxide minerals (Fig. 4d). The iron minerals show strong absorptions in the VNIR caused by various electronic processes (Hunt and Ashley, 1979). Broad charge transfer absorbs most strongly at wavelengths less than 0.5 μm although this extends up to 1.2 μm. Superimposed over this wavelength region are several crystal field absorptions, with a major band centred near 0.9 μm, which varies from 0.87 μm for hematite to 0.93 μm for goethite (Fig. 4d). Hematite was generally found in soils and unaltered metasedimentary rocks, whereas altered zones contained goethite, possibly after the weathering of pyrite.

Soil spectral signatures are very constant in shape throughout the area, and one soil spectrum is shown in Figure 4d. This shows the presence of hematite and poorly crystalline kaolinite. In the PIMA® spectral range, vegetation spectra are dominated by leaf-water and cellulose effects. The green vegetation spectrum (Fig. 4a) shows the water absorption feature at 1.92 μm and the dry vegetation spectrum shows cellulose features at 2.08 and 2.27 μm (Elvidge, 1990).

HyMap® Data Corrections

HyMap® data were acquired as radiance at the sensor. Radiance data are influenced by the solar irradiation spectrum and atmospheric effects, which include absorption (most notably by water vapor, O_2, and CO_2) and scattering by particles and gases. These effects need to be corrected because the approach used in this study was the combined use of the atmospheric removal (ATREM) radiative transfer model (Gao et al., 1993) and a spectrum-smoothing technique called EFFORT (Boardman, 1998). The result is scaled reflectance which can be compared to PIMA, field and laboratory spectral data. To obtain true reflectance, the data would need to be modeled to remove the effect of surface slope.

ATREM calculates and corrects for solar irradiance and atmospheric scattering and absorption as determined for the general conditions of the scanner survey. Atmospheric water vapor is calculated for each pixel by measuring water bands at 0.940 and 1.140 μm, but all other gases including CO_2, O_2, O_3, and CH_4 are assumed to be well mixed and fairly constant across the scene. The EFFORT process applies a gain correction to the data—the coefficients are found from the residuals that are generated by fitting a polynomial to the average of featureless image spectra. This has the effect of removing

gain effects that remain due to inaccuracies of the atmospheric correction model.

Comparisons of HyMap® pixel spectra to PIMA® spectra indicated that there was a problem with the general shape of the ATREM-EFFORT–corrected spectra. Problems with the calibration were also evident in the early processing results. An additional technique, reflectance-mean normalization (RMN), was employed (Bierwirth, 2000) to overcome these problems. This method adjusts the HyMap® band means to fit an estimated overall mean of reflectance calculated from field spectra or known end members. Representative PIMA® spectra from 16 end members (including soil and vegetation, both green and dry), together with an estimated scene-mean abundance, were used to calculate a mean reflectance spectrum for SWIR bands. Band means were then normalized to this spectrum. Examples of the comparison between laboratory, field PIMA, and the corrected HyMap® data are shown in Figure 5.

The data were also spatially aligned to satellite SPOT panchromatic data (10-m pixels) by selecting ground control points and applying a polynomial spatial correction. The SPOT panchromatic band, which measures radiance in the visible (0.51–0.73 μm), was already map registered and the spatial correction of the new airborne data allowed for the use of global positioning system (GPS) in ground follow-up and for the direct spatial comparison of processing results to the published geologic map.

Mineral Abundance Images

A combination of linear (Adams et al., 1986; Bierwirth, 1990) and partial unmixing (Boardman et al., 1995) was used to generate relative abundance images from the corrected HyMap® reflectance data. Linear unmixing involves the inversion of a matrix of known spectral end members (i.e., materials) that comprises a mixing model for a given pixel. This is essentially solving simultaneous equations where the unknowns are material abundances as proportions of a pixel. Partial unmixing also derives material abundances in a matching process that maximizes the separation of a target spectrum from the background, while suppressing the response of the composite unknown background. It must be noted that abundance values can only be considered relative, largely due to the fact that the corrected HyMap® data are scaled reflectance and that other factors are important, including grain size and intimate mixing of minerals. No comparisons of actual mineral concentrations and image abundance values have been performed for this study, although other authors suggest that lower than 3 percent mineral concentrations are detectable (Boardman et al., 1995). The results from the unmixing techniques were examined by comparing the derived abundance values to corrected image spectra and reference field and library mineral spectra. Where mineral abundances were high, spectral features for these minerals were visible in the HyMap® image spectra. After unmixing, a threshold was applied to the mineral abundances for each pixel to indicate mineral presence for display and for presentation of mineral assemblages. Minimum abundance thresholds varied for different minerals and were visually estimated as values above the image noise and where mineral features were still observable in the pixel spectra. These thresholds were applied strictly so that some lower concentrations of minerals may have been excluded.

Alteration minerals

Figure 2b shows results of HyMap® mineral abundance mapping for selected hydrothermal alteration minerals found in the Indee district. Threshold values indicating presence were estimated and applied to each of five mineral end members. Combinations of sets of two minerals are also shown and the term "sericite" combines Al-poor and Al-rich white mica. Fe chlorite is an alteration mineral but is also present in metamorphic and weathered basic rocks. The other minerals in Figure 2b are exclusively hydrothermal in origin in this area. Pyrophyllite and white mica are present in auriferous systems within the Mallina shear zone (Fig. 2). Pyrophyllite in area A (Fig. 2) encompasses the Camel 2 prospect, one of the three

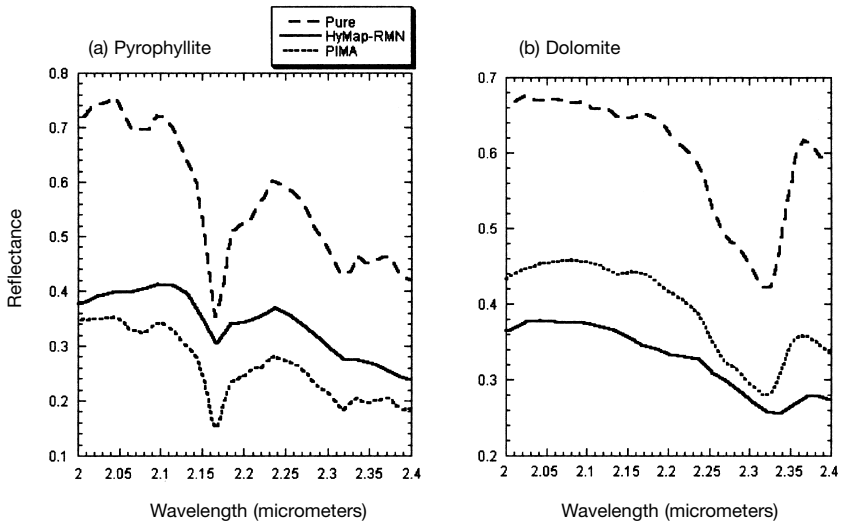

FIG. 5. Comparison of a pure mineral spectrum (USGS spectral library), PIMA data for a field sample, and the corresponding RMN-corrected HyMap® pixel spectrum for pyrophyllite and dolomite over part of the SWIR spectral range.

major known deposits in the Indee district. Pyrophyllite is the most significant alteration product at this deposit (Huston et al., 2002a).

Area B (Fig. 2) represents a possible new prospect based on the occurrence of previously unknown pyrophyllite. The presence of pyrophyllite here was confirmed by PIMA analysis of field samples. A comparison of the distribution of minerals (Fig. 2b) to the geology (Fig. 2a) shows that area B is partly covered by calcrete and sand. The target area is flat and contains very little outcrop (Fig. 3a), with only soil and rock float at the surface, which is interpreted to be thin (<1 m) and in situ. This pyrophyllite occurrence corresponds closely with the interpreted location of the Mallina shear zone from geophysical data. Elevated gold (0.34 ppm) in a composite grab sample of several rocks collected from this area indicates possible along-strike continuation of mineralization. Another pyrophyllite occurrence to the south-east of area C (Fig. 2) has not been investigated but may also be prospective, based on the presence of hydrothermal alteration mineralogy.

The Becher prospect (D, Fig. 2b) is spatially associated with low Al white mica and tourmaline. X-ray diffraction confirms the presence of tourmaline and the PIMA® spectral analysis indicates a schorl composition. As with area B, area C also returned an anomalous gold assay (0.1 ppm) from a grab sample. Another potential target is a small zone of tourmaline adjacent to low Al white mica (E, Fig. 2b)

The Al content of white mica (sericite) is indicated by the wavelength position of the AlOH absorption feature (Duke, 1994). Longer wavelengths indicate lower Al content and this can relate to cooler temperatures of formation (Duke, 1994). This is consistent with observations in the Indee district (Fig. 2b) where Al-poor white mica (absorption feature at 2.210 μm) is associated with lower temperature epithermal-like veins, whereas high Al white mica (feature at 2.194 μm) is associated with higher temperature lode Au systems and metamorphic assemblages. High Al compositions of white mica are common in higher temperature ore zones (Huston and Kamprad, 1998; Yang et al, 1999; Cudahy et al., 2000), although others can be dominated by low Al phengite (Li et al., 1998). The white mica mineralogy may also reflect the chemistry of the host rocks (Cathelineau, 1988) and the nature of the hydrothermal fluids (Parry et al., 1984). Importantly, in the Mallina area, the presence of phengitic white mica distinguishes some of the hydrothermal alteration from the surrounding metamorphic rocks, making HyMap® a powerful predictive tool for mineral exploration.

Regolith minerals

Regolith minerals and assemblages are shown in Figure 2c. These surface materials are difficult to map in the field because individual minerals cannot be readily identified in the regolith. Calcretes range in composition from dolomite to calcite. Dolomite is associated with calcretized bedrock, whereas calcite is dominant in soil-covered areas or calcretized basic rocks. These different calcrete associations and types are not separated in the map (Fig. 2a). On the ridge in the southeast of the area, dolomite grades to calcite with increasing distance away from the ridge. This is interpreted to be a function of decreasing bedrock exposure. Calcite is also present locally in altered bedrock (not calcretized) and veins in hydrothermal areas.

High goethite concentrations (Fig. 2c) are related to gossans associated with mineralization (e.g., areas A and C), ironstones in the sediments, and ferricretes. Ferricretes are deposits of iron hydroxides and oxyhydroxides formed within the regolith by precipitation from ground waters. Some ferricretes are a mixture between goethite and hematite. Although not extensively investigated, some goethite shown in Figure 2c is potential gossanous exploration targets and many of these may correlate with bedrock hydrothermal minerals (Fig. 2b).

Highest concentrations of hematite and kaolinite, in association and individually, are commonly found in areas of high chlorite abundance (see Fig. 2b) as a result of weathering of the outcrop. Although kaolinite and hematite are pervasive throughout the area in sandy soils, lower concentrations are masked by thresholds applied in Figure 2c. Also, the lower crystallinity of soil kaolinite means that the 2.162-μm feature is less defined (see Fig. 4), resulting in lower kaolinite abundances.

Knowledge of the regolith, and its mineralogy, is also important for placing soil geochemical data in context. For example, at Indee, areas of calcrete composed of calcite (Fig. 2c) indicate where bedrock is not exposed. These calcretes could be used as sampling media to explore the subtle geochemical effects of underlying mineralization.

Conclusions

This study shows that HyMap® hyperspectral data can be used to effectively map alteration minerals associated with gold prospects, even in poorly exposed terrane, as long as the regolith is in situ. Moreover, the mineral maps can be used to identify the type of prospect based on associated alteration assemblages. Mineral maps generated using the HyMap® data successfully identified the location of the Camel 2 Au prospect, which is associated with pyrophyllite-bearing assemblages, and the Becher prospect, which is associated with sericitic alteration assemblages. More importantly, the mineral mapping identified two additional mineral anomalies, both of which returned anomalous gold in rock chips. The HyMap® mineral mapping also identified zones of tourmaline alteration, which may be of significance as a proximity indicator of mineralization. However, the HyMap® mineral mapping did not identify the Withnell lode Au deposit, possibly because the alteration assemblages are similar to the regional metamorphic assemblage.

The HyMap® data indicate that compositional differences in white mica, which relate to deposit type, can also be mapped. Deposits along the Mallina shear zone, such as Camel 2, are associated with pyrophyllite and Al-rich white mica. In contrast, epithermal-like systems south of the shear zone (e.g., Becher) were characterized by Al-poor white mica and possibly tourmaline.

This study shows that hyperspectral mineral abundance maps can successfully delineate the distribution of primary, hydrothermal, metamorphic, weathering, and residual regolith minerals in an area characterized by low relief, poor exposure, calcretization, and extensive bedrock weathering.

Acknowledgments

Thanks are due to Resolute Limited for access and field support in the Indee study area. Tom Cudahy of CSIRO

Division of Exploration and Mining, Perth, provided general assistance and loan of the PIMA® instrument. This paper is a contribution to the North Pilbara National Geoscience Mapping Accord Project (1995–2000). DH and RB publish with permission of the Chief Executive Officer, Geoscience Australia.

REFERENCES

Adams, J.B., Smith, M.O., and Johnson, P.E., 1986, Spectral mixture modelling: A new analysis of rock and soil types at the Viking Lander 1 site: Journal of Geophysical Research, v. 91, p. 8098–8112.

Australian Registry of Mining, 2001, Register of Australian Mining 2000/2001: Perth, Resource Information Unit, 672 p.

Bierwirth, P.N., 1990, Mineral mapping and vegetation removal via data-calibrated pixel unmixing using multispectral images: International Journal of Remote Sensing, v. 11, p. 1999–2017.

——2000, Hyperspectral mineral mapping and gold prospecting in a low bedrock-exposure terrain using HyMap in the West Pilbara, W.A.: Australasian Remote Sensing Conference, Adelaide, 10th, Proceedings, Paper 56, p. 814–825 [CD-ROM].

Blewett, R.S., 2002, Archaean tectonic processes: A case for horizontal shortening in the North Pilbara granite-greenstone terrane, Western Australia: Precambrian Research, v. 113, p. 87–120.

Boardman, J.W., 1998, Post-Atrem polishing of AVIRIS apparent reflectance data using EFFORT: A lesson in accuracy versus precision: Jet Propulsion Laboratory AVIRIS Earth Science Workshop, 7th, Publication 97-21, Summaries, p. 53–57.

Boardman, J.W., Kruse, F.A., and Green, R.O., 1995, Mapping target signatures via partial unmixing of AVIRIS data: Jet Propulsion Laboratory AVIRIS Earth Science Workshop, 5th, Publication 95-1, Summaries, p. 23–26.

Cathelineau, M., 1988, Cation site occupancy in chlorites and illites as a function of temperature: Clay Minerals, v. 23, p. 471–485.

Cocks, T., Jenssen, R., Stewart, A., Wilson, I., and Shields, T., 1998, The HyMap airborne hyperspectral sensor: The system, calibration and performance: EARSEL Workshop on Imaging Spectrometry, 1st, Zurich, October, EARSEL, 1998, Proceedings, p. 37–43.

Cudahy, T.J., Okada, L., and Brauhart, C., 2000, Targeting VMS-style Zn mineralisation at Panorama, Australia, using airborne hyperspectral VNIR-SWIR HyMap data: Environmental Research Institute of Michigan, International Conference on Applied Geologic Remote Sensing, 14th, Las Vegas, Nevada, Proceedings, p. 395–402.

Duke, E.F., 1994, Near infrared spectra of muscovite, Tschermak substitution, and metamorphic reaction progress: Implications for remote sensing: Geology, v. 22, p. 621–624.

Elvidge, C.D., 1990, Visible and near infrared reflectance characteristics of dry plant materials: International Journal of Remote Sensing, v. 11, p. 1775–1795.

Gao, B., Heidebrecht, K.B., and Goetz, A.F.H., 1993, Derivation of scaled surface reflectances from AVIRIS data: Remote Sensing of Environment, v. 44, p. 165–178.

Hunt, G.R., and Ashley, R.P., 1979, Spectra of altered rocks in the visible and near infrared: Economic Geology, v. 74, p. 1613–1629.

Huston, D.L., and Kamprad, J., 1998, Alteration zonation and geochemical dispersion at the Western Tharsis deposit, Mt. Lyell, Tasmania: A summary, *in* Studies of VHMS-related alteration: Geochemical and mineralogical vectors to ore: Australian Mineral Industry Research Association/Australian Research Council project P439, p. 125–128.

Huston, D.L., Blewett, R.S., Keillor, B., Standing, J., Smithies, R.H., Marshall, A., Mernagh, T.P., and Kamprad, J., 2002a, Lode gold and epithermal deposits of the Mallina basin, North Pilbara terraun, Western Australia: Economic Geology, v. 97, p. 801–818.

Huston, D.L., Sun, S-S., Blewett, R., Hickman, A., Van Kranendonk, M., Phillips, D., Baker, D., and Brauhart, C., 2002b, The timing of mineralization in the Archean North Pilbara terrain, Western Australia: Economic Geology, v. 97, p. 733–755.

Li, X., Kwak, T.A.P., and Brown, R.W., 1998, Wall-rock alteration in the Bendigo gold ore field, Victoria, Australia: Uses in exploration: Ore Geology Reviews, v. 13, p. 381–406.

McLeod, R.L., Gabell, A.R., Green, A.A., and Gardavski, V., 1987, Chlorite infrared spectral data as proximity indicators of volcanogenic massive sulphide mineralisation: Pacific Rim Congress 87, Gold Coast, 1987, Proceedings, p. 321–324.

Parry, W.T., Ballantyne, J.M., and Jacobs, D.C., 1984, Geochemistry of hydrothermal sericite from Roosevelt Hot Springs and the Tintic and Santa Rita porphyry copper systems: Economic Geology, v. 79, p. 72–86.

Smithies, R.H., 1999, Geology of the Yule 1:100,000 sheet: Western Australia Geological Survey, 1:100,000 series explanatory notes, sheet 2556, 15 p.

Van Kranendonk, M.J., Hickman, A.H., Smithies, R.H., Nelson, D.R., and Pike, G., 2002, Geology and tectonic evolution of the Archean North Pilbara terrain, Pilbara Craton, Western Australia: Economic Geology, v. 97, p. 695–732.

Yang, K., Huntington, J.F., Boardman, J.W., and Mason, P., 1999, Mapping hydrothermal alteration in the Comstock mining district, Nevada, using simulated satellite-borne hyperspectral data: Australian Journal of Earth Sciences, v. 46, p. 915–922.